

Article

Development of Nickel-BTC-MOF-Derived Nanocomposites with rGO Towards Electrocatalytic Oxidation of Methanol and Its Product Analysis

Lubna Yaqoob ¹, Tayyaba Noor ^{2,*}, Naseem Iqbal ³ , Habib Nasir ¹  and Neelam Zaman ¹

¹ School of Natural Sciences (SNS), National University of Sciences and Technology (NUST), Islamabad 44000, Pakistan; lubnayaqoob96@gmail.com (L.Y.); habibnasir@sns.nust.edu.pk (H.N.); neelamzaman6650@gmail.com (N.Z.)

² School of Chemical and Materials Engineering (SCME), National University of Sciences and Technology (NUST), Islamabad 44000, Pakistan

³ U.S.-Pakistan Centre for Advanced Studies in Energy (USPCAS-E), National University of Sciences and Technology (NUST), Islamabad 44000, Pakistan; naseem@uspcase.nust.edu.pk

* Correspondence: tayyaba.noor@scme.nust.edu.pk; Tel.: +92-51-9085-5121

Received: 16 September 2019; Accepted: 8 October 2019; Published: 14 October 2019



Abstract: In this study, electrochemical oxidation of methanol to formic acid using the economical and highly active catalytic Nickel Benzene tricarboxylic acid metal organic framework (Ni-BTC-MOF) and reduced graphene oxide (rGO) nanocomposites modified glassy carbon electrode GCE in alkaline media, which was examined via cyclic voltammetry technique. Nickel based MOF and rGO nanocomposites were prepared by solvothermal approach, followed by morphological and structural characterization of prepared samples through X-ray diffraction (XRD), scanning electron microscopy (SEM), Fourier Transform Infrared Spectroscopy (FTIR), and energy dispersive X-ray (EDX) analysis. The electrochemical testing of synthesized materials represents the effect of the sequential increase in rGO concentration on electrocatalytic activity. The Ni-BTC/4 wt % rGO composite with a pronounced current density of 200.22 mA/cm² at 0.69 V versus Hg/HgO electrode at 50 mV/s was found to be a potential candidate for methanol oxidation in Direct Methanol Fuel Cell (DMFC) applications. Product analysis was carried out through Gas Chromatography (GC) and Nuclear Magnetic Resonance (NMR) spectroscopy, which confirmed the formation of formic acid during the oxidation process, with approximately 62% yield.

Keywords: MOF/rGO nanocomposites; Ni-BTC; rGO; methanol oxidation; direct methanol fuel cell

1. Introduction

The human appetite for energy is constantly growing and becoming increasingly difficult to satiate. Currently, the world's enormous energy demands are mainly met by nonrenewable and environmentally unfriendly fossil fuels; however, the development of vital energy sources for an increasingly thriving world to mitigate fossil fuel resource depletion and environmental pollution are pressing issues for society right now [1,2]. Invention of numerous nonconventional means to bridge the gap between energy demand and supply is the utmost requirement of the modern era. Fuel cells, an alternate to fossil fuels, are now emerging as a robust and modest source of renewable energy, as well as an immaculate, efficient, and benign method for energy conversion [3,4].

To date, a variety of fuel cells are available that are divergent in their operating temperature, electrical efficiency, power output, and typical applications. Among these different fuel cells, direct methanol fuel cells (DMFCs) are a remarkable option for portable devices and light duty vehicles because of their high energy density, inexpensive nature, reduced corrosion, easy handling of liquid

fuel, and low temperature requirements [5]. A critical approach for aspirational sustainable energy sources is the fabrication of highly proficient, green, economical catalysts for energy conversion and storage applications [6]. Electrochemical oxidation of methanol in fuel cell leads to different products; for instance, CO_2 , HCHO, HCOOH, and CO depend on reaction temperature, the reactant's partial pressure, and most importantly, the nature of the catalyst [7]. Hydrogen and water are generated as side products, where hydrogen is further utilized as an energy source for fuel cells. Gaseous products, such as CO and CO_2 , are released to the atmosphere, while formic acid is effectively utilized as a preservative, antibacterial agent, and for treatment of warts. It is also used in the production of leather, rubber, and esters, in addition to being used as a solvent in HPLC. Methanol oxidation, an anodic half-cell reaction of direct methanol fuel cells, is catalyzed by highly efficient Pt catalysts in acidic media [8,9]. However, formation of poison intermediates, such as HCHO and CO, and their strong binding with Pt, is responsible for sluggish kinetics. Alkaline electrolytes prove to be better alternatives in view of their increased current density at particular potentials, their potential shift toward lower voltage, reduced catalyst loading, strong binding of catalysts to metal sites, as well as the stability of cheaper non-noble metal catalysts in alkaline media [10–12].

Until now, extensive research work has been done to modify Pt-based catalysts to optimize the methanol oxidation process. Platinum-based nanorods; nanoflowers; nanocubes; composites of Pt with metal oxides, such as Fe_2O_3 , TiO_2 , SnO_2 , Cu_2O , ZnO ; as well as conductive polymer support-based Pt catalysts, with enhanced electrical conductivity and reduced charge transfer resistance, have been extensively studied for methanol oxidation [13–17]. Furthermore, carbon based materials, such as carbon powder, CNTs, graphene, graphene oxide, and reduced graphene oxide, are potential candidates for this application because of their increased surface area, high conductivity, thermal stability, reduced catalytic poisoning, and elevated charge carrier mobility. Among these carbon-based materials, graphene is the best option because of its large surface area, conductivity, and enhanced electron and mass transport, while rGO is preferred over GO because of its increased conductivity [18–21].

In recent decades, metal–organic frameworks have moved to the forefront as novel crystalline materials, extending from one dimensional (1D) to three dimensional (3D). Their huge surface area, porosity, and stability are effectively utilized for energy conversion, gas separation and storage, and catalysis, in addition to being used in sensors and for biological applications [22–24]. Limited applications of MOFs for electrocatalysis, because of their constrained charge transfer and dejected electrical conductivity, can be overcome by combining them with conductive materials, such as with CNTs, carbon nanowire, reduced graphene oxide, or graphene, transforming them into potential candidates for electrochemical processes, such as oxygen reduction reactions (ORR), hydrogen evolution reactions (HER), oxygen evolution reactions (OER), CO_2 reduction, methanol oxidation, and photocatalysis [25–32]. Furthermore, MOFs and their derived compounds act as efficient catalysts for evolution reactions during the redox process in fuel cells or water decomposition [33,34].

In this work, we synthesized Ni-BTC-MOF/rGO composites using the solvothermal method and investigated their electrocatalytic capacity for methanol oxidation in alkaline medium. The interconversion of Ni in different oxidation states, its resistance toward poisonous intermediates, and its extraordinary stability make nickel an attractive and appealing candidate for methanol oxidation [35]. Moreover, the greater surface area, additional stability, and improved electrical conductivity provided by incorporation of rGO into MOF play important roles in enhancing the electrocatalytic activity of synthesized materials [36–38]. To the best of our knowledge, the electrocatalytic response of Ni-BTC-MOF/rGO composites for methanol oxidation, along with qualitative and quantitative product analysis, has not been reported in literature to date.

2. Results and Discussion

To attain Ni-BTC-MOF/rGO, a solvothermal method was used for the synthesis. In order to prepare Ni-BTC composites with rGO, a sequence of experiments was performed with varying amounts of rGO. All these experiments were executed by using 2 g $\text{Ni}(\text{NO}_3)_2 \cdot 6\text{H}_2\text{O}$ and 1 g of 1,3,5 benzene

tricarboxylic acid (linker), with an appropriate amount of rGO added to the mixture of solvents C_2H_5OH and Dimethylformamide (DMF). The homogenous mixture was then transferred to a 50 mL Teflon-lined autoclave and kept in the oven at $85\text{ }^\circ\text{C}$ for 24 h. The prepared solid material was collected, washed with solvents, and dried at $65\text{ }^\circ\text{C}$ for 24 h (see Material and Methods section for further details). Ni-BTC-MOF and 1–5 wt % rGO composites of MOF were characterized by employing FTIR, EDX, XRD, and SEM analysis.

The crystalline nature of the synthesized materials revealed through powdered XRD is illustrated in Figure 1a, where the sharpness of peaks depicts the crystallinity of synthesized materials. Diffraction peaks at 23° (004) and 17° (002) are ascribed to the crystal plane of rGO and partial reduction of the GO peak, which is enhanced in 5 wt%, but these peaks are not highly significant in other composites [39]. This may be caused by overlapping of significant peaks of metals at this scale because of their crystalline nature, and also may give an indication that rGO did not interfere in metal–ligand interactions [40]. Peaks at 10° (211), 15° (321), and 24.5° (600) may be caused by localized metal oxides and hydroxide formation [41]. Peaks at 2θ values of 35° (022), 42° (512), and 51° (226) indicate the presence of nickel [42]. The XRD pattern for synthesized samples is identical to the reported and simulated pattern [43,44].

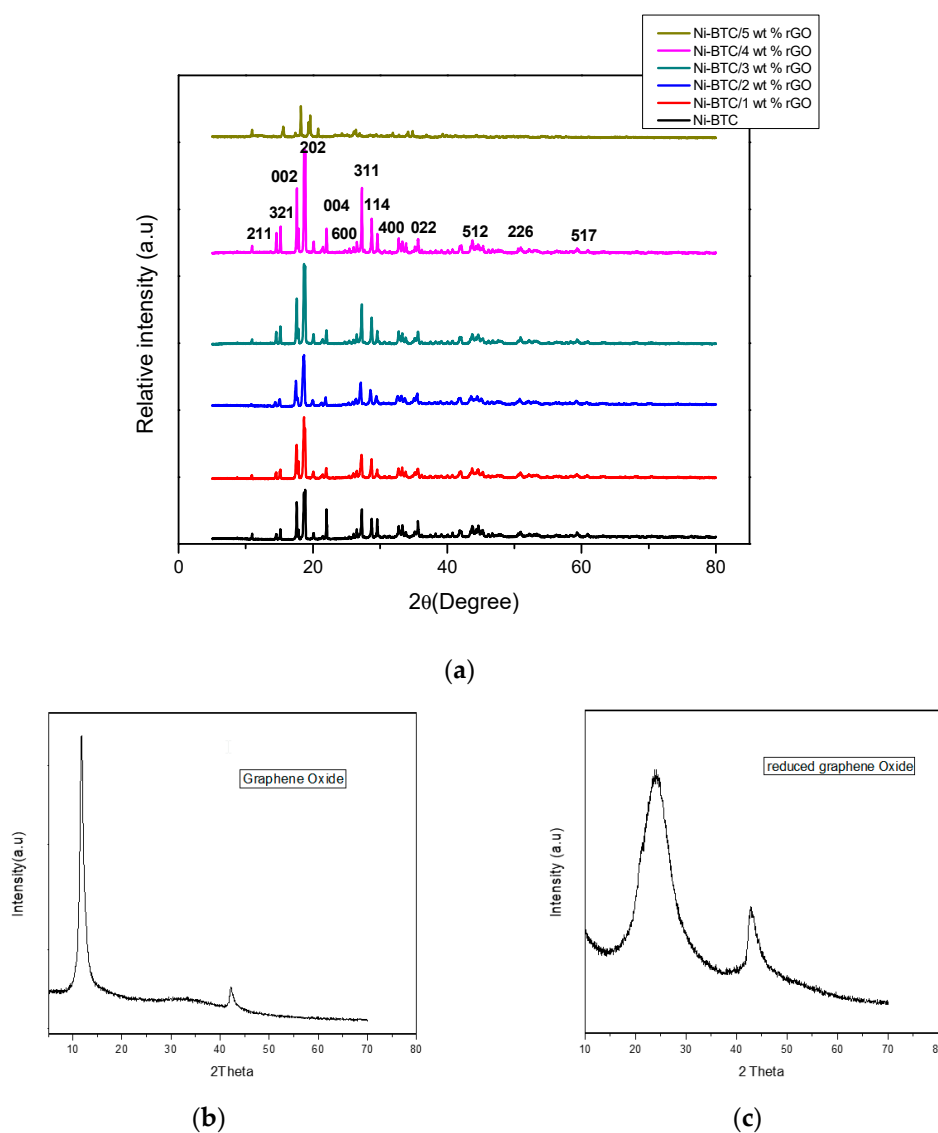


Figure 1. X-ray diffraction (XRD) pattern of (a) Ni-BTC-MOF and 1–5 wt % rGO composites (b) GO and (c) rGO.

Figure 1b illustrates the XRD pattern of graphene oxide. At the 2θ value of 10.5° with 0.841 nm d spacing, a sharp peak proves the graphene oxide formation. At the 2θ value of 42.2° with d spacing of 0.212 nm, a less intense peak appears, caused by the presence of unexfoliated graphite.

Figure 1c illustrates the XRD pattern of reduced graphene oxide. At the 2θ value of 25.4° with 0.4 nm d spacing, the broad peak corresponds to reduced graphene oxide formation. At the 2θ value of 42.5° with d spacing of 0.21 nm, a less intense peak appears caused by the presence of unexfoliated graphite [45].

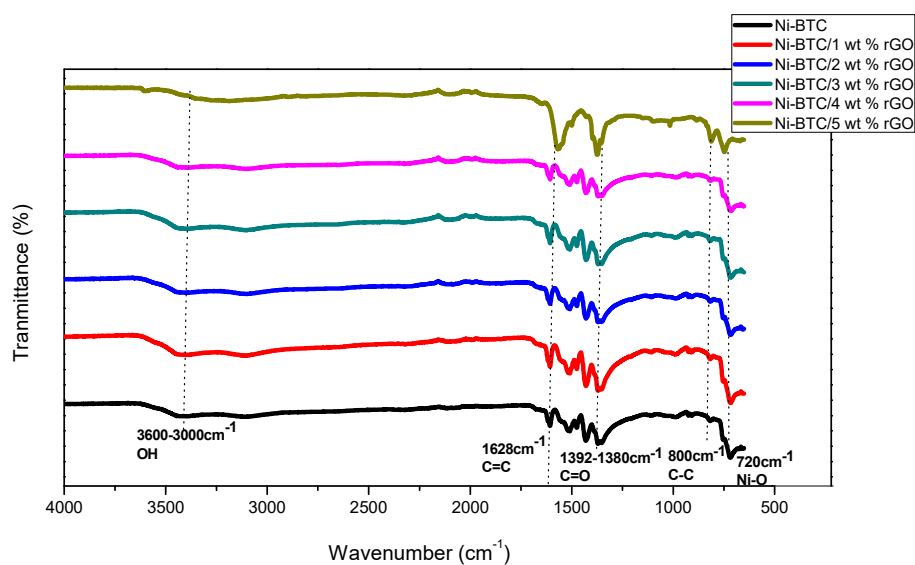
In the FTIR spectrum of GO, strong absorption bands caused by the stretching vibration of hydroxyl O–H, carbonyl C=O, and carbon to carbon double bond C=C appear at 3200 cm^{-1} , 1722 cm^{-1} , and 1622 cm^{-1} , respectively, while epoxy and alkoxy groups give stretching vibration peaks at 1220 cm^{-1} and 1048 cm^{-1} , respectively. Reduction of oxygen-containing functional groups on the surface of GO by hydrazine hydrate is illustrated in the FTIR spectrum of rGO by the disappearance of peaks at 1722 cm^{-1} and 1220 cm^{-1} , while the presence of O–H functional groups (O–H) with low intensities cause a peak at 3247 cm^{-1} , further confirming sp^2 lattice recovery with a peak at 1650 cm^{-1} [46].

The functional groups' presence in Ni-BTC-MOF/rGO was verified with the help of FTIR, as illustrated in Figure 2a. The stretching vibrations of OH groups of physically adsorbed water show a broad adsorption band in the range of $3600\text{--}3000\text{ cm}^{-1}$ [43,47,48]. The absence of significant peaks in the region of $1800\text{--}1680\text{ cm}^{-1}$, as well as deviation of peaks from 1715 to 1608 cm^{-1} , clearly indicate complete deprotonation of the COOH group of benzene tricarboxylic acid (BTC) ligands and the linking of ligands with metals, which is further proved by the metal–ligand peak at 720 cm^{-1} [44,49]. Furthermore, the distinctive bands of the COOH group caused by asymmetric and symmetric vibrations appear in the ranges of $1645\text{--}1550\text{ cm}^{-1}$ and $1470\text{--}1390\text{ cm}^{-1}$, respectively. The C=C stretching vibration leads to a strong absorption band at 1628 cm^{-1} in Ni-BTC/5 wt % rGO, and a less intense peak in other composites (i.e., Ni-BTC/1–4 wt % rGO and pure Ni-BTC). The covalent interactions of an organic linker strongly alter the extended aromatic character of rGO through conversion of carbon atoms from sp^2 to sp^3 hybridization, which results in a decrease of $\text{sp}^2\text{--C=C}$ bond absorption frequency (i.e., stretching). However, in this case, the peak intensity of sp^2 carbon atoms is increased. These results clearly reveal the lack of covalent interaction between rGO and Ni-BTC-MOF [50]. A peak at $1392\text{--}1380\text{ cm}^{-1}$ corresponds to C=O, showing symmetric stretching. The following peaks also reflect metal deprotonation with ultimate linking of metal with oxygen and successful synthesis of composites [51,52]. While the peaks at 800 cm^{-1} caused by C–C stretching vibration and out-of-plane deformation vibration of the C–H group in the benzene ring are present in all samples, their intensity is higher in the 5 wt % sample because of its high rGO content [50].

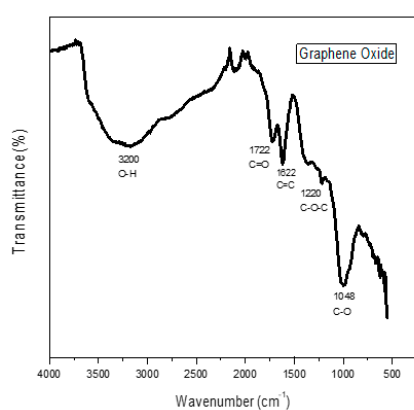
The Raman spectrum of GO illustrated in Figure 3a gives an idea of the existent structural defects of the graphene layer. Two characteristic bands that appear in the GO spectrum are D and G bands. The D band displayed at 1352 cm^{-1} is caused by the stretching vibration of aromatic C=C, while the G band visible at the 1600 cm^{-1} position develops because of the transformation of the sp^2 hybridized carbon of the ring system to sp^3 hybridized carbon, as well as owing to available oxygen-bearing functional groups on the surface of GO.

The intensity ratio of D and G bands (0.92), depicting structural defects and disorder, is clear evidence of oxidation of graphite. On the same grounds, the D band of rGO at 1348 cm^{-1} and G band at 1595 cm^{-1} in (Figure 3b) appear to be caused by structural defects and stretching vibration of sp^2 hybridized C=C in aromatic groups, respectively. The I_D/I_G ratio obtained in this case is 1.42, which reveals insufficient structural recovery of rGO and existence of sp^3 after functionalization [53,54].

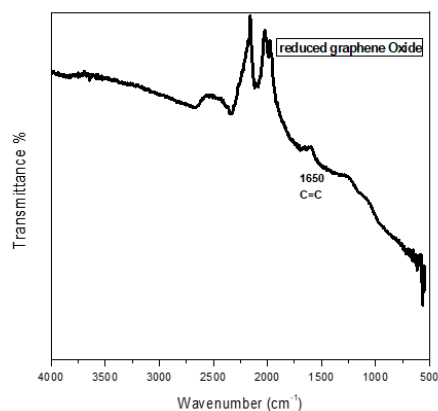
The crystal structure and morphology analysis performed through SEM confirm that the hexagonal, rod-like structures in all synthesized materials (Figure 4a) closely match with reported literature [42]. Moreover, rGO flakes are also clearly visible in prepared composite materials, present between MOF crystals (Figure 4b–g).



(a)

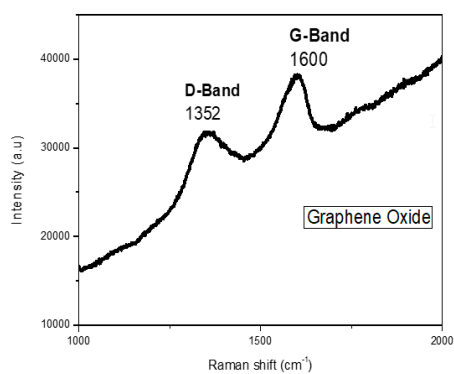


(b)

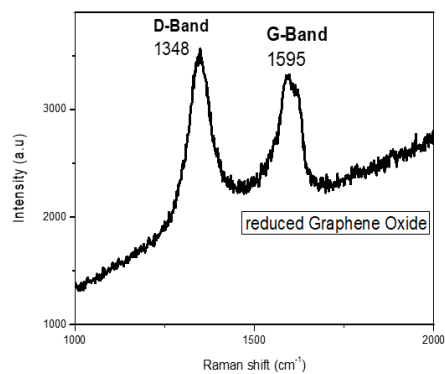


(c)

Figure 2. FTIR spectrum of (a) Nickel Benzene tricarboxylic acid (Ni-BTC) MOF and 1–5 wt % rGO composites (b) GO and (c) rGO.



(a)



(b)

Figure 3. Raman IR analysis of (a) GO and (b) rGO.

The elemental analysis using EDX confirmed the presence of carbon, oxygen, as well as Ni in all prepared samples, without any impurities, as shown in Table 1. Furthermore, the gradual increase in rGO concentration leading to elevated carbon and oxygen percentages confirms the successful incorporation of rGO into the MOF structure.

Table 1. Energy Dispersive X-rays (EDX) analysis of Ni-BTC-MOF and 1–5 wt % rGO composites.

Sample Element	Ni-BTC	Ni-BTC/1 wt % rGO	Ni-BTC/2 wt % rGO	Ni-BTC/3 wt % rGO	Ni-BTC/4 wt % rGO	Ni-BTC/5 wt % rGO
C wt %	35.66	39.66	42.13	45.65	53.11	53.69
O wt %	26.89	29.05	36.99	41.88	39.67	41.06
Ni wt %	37.45	31.29	20.92	12.48	7.22	5.25

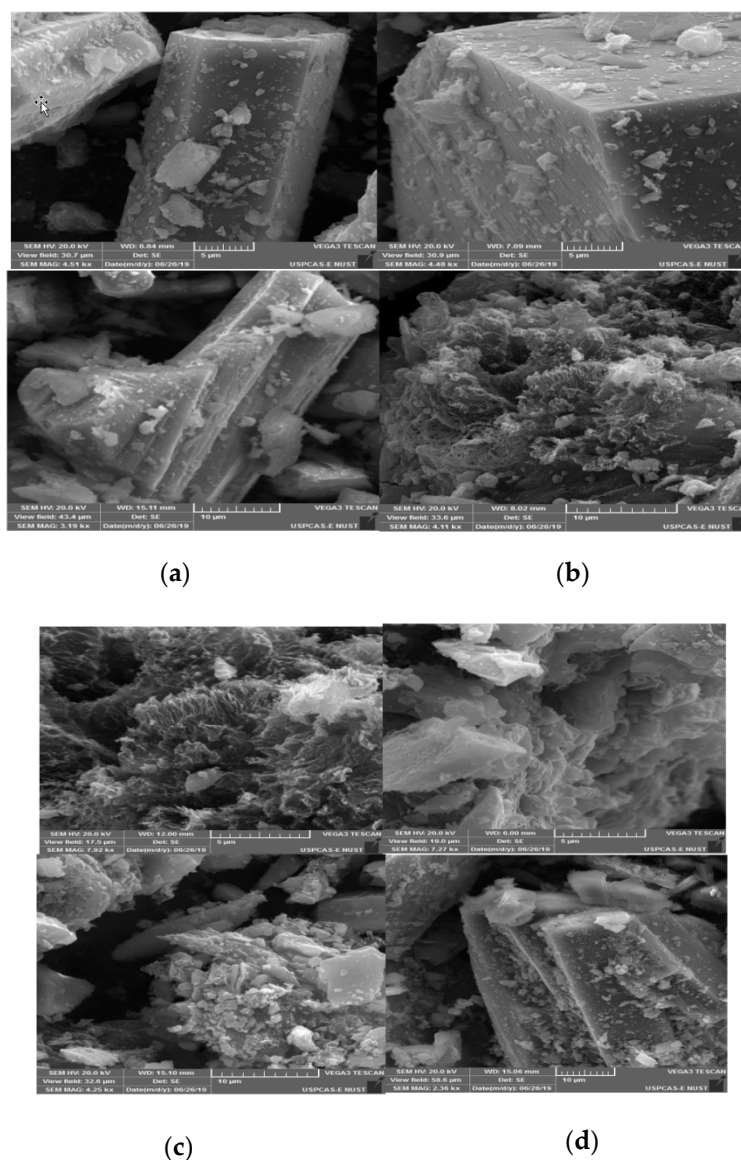


Figure 4. Cont.

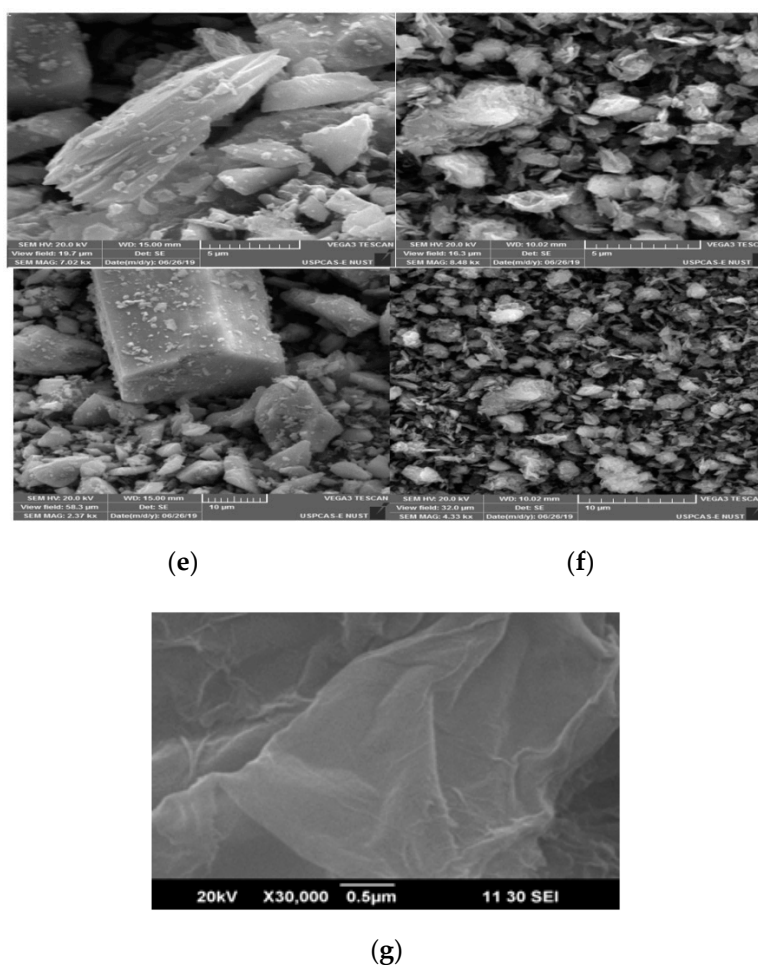


Figure 4. SEM images of (a) Ni-BTC-MOF, (b) Ni-BTC/1 wt % rGO, (c) Ni-BTC/2 wt % rGO, (d) Ni-BTC/3 wt % rGO, (e) Ni-BTC/4 wt % rGO, (f) Ni-BTC/5 wt % rGO, and (g) rGO.

2.1. Electrochemical Measurements

The electrochemical measurements were pursued through Potentiostat (CH Instruments Inc, CHI 760, Austin, TX, USA). During the experiment, a NaOH-saturated Hg/HgO electrode was used as a reference electrode; platinum wire acted as a counter electrode, while a glassy carbon electrode was selected as the working electrode. Catalyst ink was prepared by mixing 2 mg catalytic material into 3 μL of 5 wt% Nafion solution, which has excellent binding properties and electrical conductivity, along with 97 μL ethanol solvent. In order to analyze the methanol oxidation catalytic activity of synthesized samples, all electrochemical measurements were performed between -0.1 V and 0.7 V at different scan rates. At first the data was collected with bare electrodes, and then subsequently with catalyst-deposited Glassy Carbon electrode (GCE) electrodes. Electrochemical impedance spectroscopy (EIS) measurements were performed within a frequency range of $1-1 \times 10^5$ Hz and an amplitude 0.005 V in a three-electrode system, while the stability of the catalysts was tested at a peak potential 0.69 V with chronoamperometric experiments. Qualitative and quantitative analysis of the product was performed through bulk electrolysis, followed by data acquisition via GC and NMR.

2.2. Preparation of Working Electrodes

In order to formulate modified GCE electrodes for CV, Tafel plots, EIS, and chronoamperometric measurements, catalytic ink was prepared by mixing 2 mg catalyst, 3 μL Nafion, and 97 μL ethanol. Then, 3 μL of homogenous mixture (1.07 mg/cm² catalyst) was mounted through micropipette on GCE,

followed by drying under an infrared lamp. Complete analysis of synthesized samples was carried out at different scan rates within a voltage window ranging from -0.1 to 0.7 V.

The catalytic activity tests for MOF and their respective rGO composites were carried out with an electrochemical workstation (CHI 760E, CH Instruments, Austin, TX, USA) at room temperature using a standard three-electrode system, with 1 M NaOH aqueous solution used as a supporting electrolyte solution. The Hg/HgO electrode and Pt wire were used as reference and counter electrodes, respectively, while GCE was used as a working electrode. Cyclic voltammetry was performed to optimize the catalyst amount. Different amounts of catalysts ranging from 0.25 mg to 3.5 mg were loaded on the surface of GCE by drop cast method with a potential sweep between -0.1 V and 0.7 V in an alkaline electrolyte solution. The current density increased gradually in line with the increase of catalyst amount until 2 mg, which was found to be the ideal concentration for further analysis, as shown in Figure 5a.

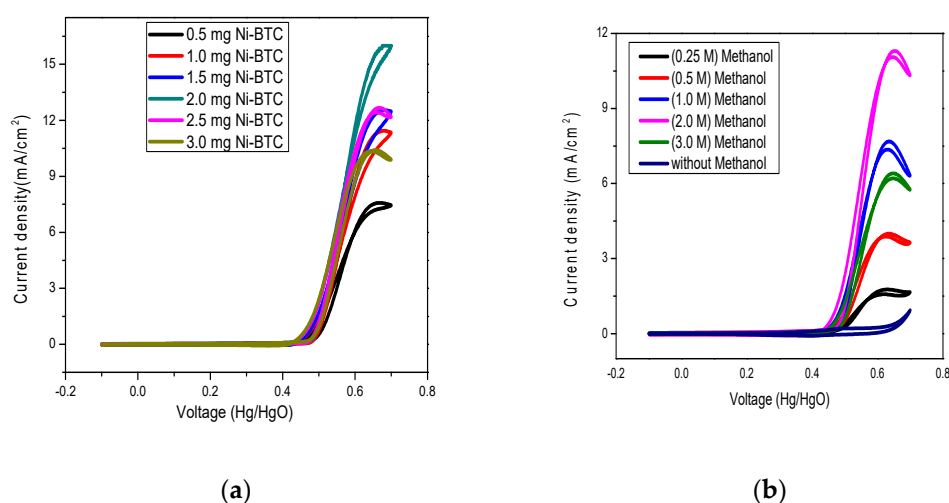


Figure 5. (a) Effects of catalyst load amount and (b) different molarities of methanol on current density.

On the same grounds, the range between 0.25 M and 3.0 M methanol was tested for optimization, with 2 M methanol selected for further experimentation, as indicated in Figure 5b.

From Figure 6a, it is clear that the current density shown by Ni-BTC-MOF at 50 mV/s is only 27.155 mA/cm², while the current densities possessed by 1 – 4 wt % rGO composites are 86.346 mA/cm², 112.035 mA/cm², 125.829 mA/cm², and 200.22 mA/cm², respectively; the 5 wt % rGO composite current density tends to be lower. From the results it is clear that incorporation of rGO is responsible for the increase in current density for 4 wt % rGO composites, which then decreases, as illustrated in Figure 6b. The main reason behind this is the development of additional pores in the already developed porous structure of Ni-BTC-MOF, dispersion of MOF nanoparticles on the surface of rGO, easy availability of active sites, and the enhanced surface area of the composites [55–57]. Ni-BTC-MOF/ 4 wt % rGO composite is the most efficient catalyst for methanol oxidation, as rGO's excellent thermal stability, enhanced electrical conductivity, and tendency to mitigate aggregation provides a huge surface area and good conductivity by minimizing charge transfer resistance [58]. The Ni-BTC/ 5 wt % rGO composite comparatively shows a reduced current density of 60.727 mA/cm², as shown in Figure 6b, which could be caused by accumulation of charges on the rGO surface and blockage of active sites because of rGO aggregation [41].

Cyclic voltammetry was performed by potential sweep technique between -0.1 V and 0.7 V at a scanning speed of 5 – 50 mV/s in an alkaline electrolyte to study the effect of scan rate, as demonstrated in Figure 7. These results reveal that by increasing the scan rate from 5 – 50 mV/s, the current density increases in all composites. This behavior can be attributed to the fact that with the increase of scan rate, more electroactive species reached the electrode surface, leading to high current density [59].

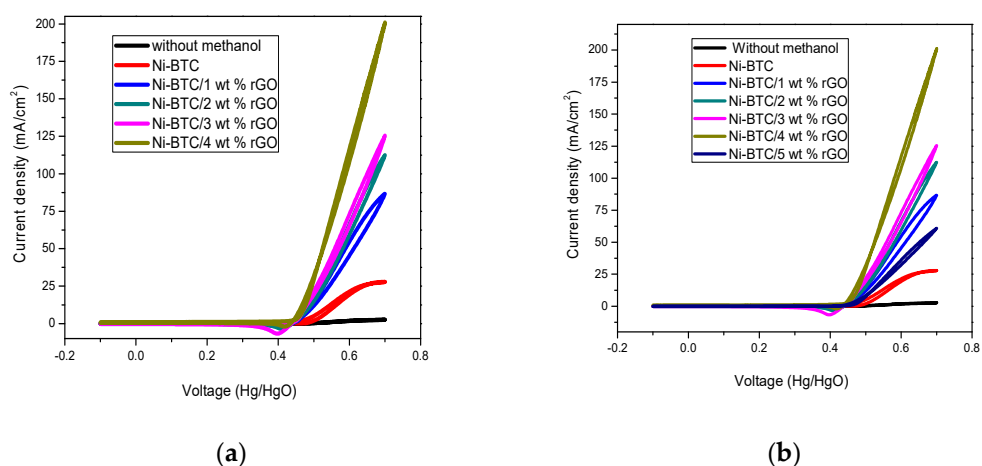


Figure 6. (a) Comparison of current density of Ni-BTC-MOF and 1–4 wt % rGO composites and (b) Ni-BTC-MOF and 1–5 wt % rGO composites in 1 M NaOH and 2 M methanol solution at a scan rate of 50 mV/s.

Figure 8 show the direct relationship between peak current density and square root of scan rate, where diffusion coefficient is proportional to slope of the straight line. Therefore, by determining the linearity of the plot, it is possible to calculate the charge transfer coefficient (α), as well as the diffusion coefficient (D). The diffusion coefficient is calculated by employing the Randles–Sevcik equation [55], with the area (A) of the electrode shown in cm² and the concentration (C) of methanol shown in mole/dm³.

$$I_p = (2.99 \times 10^5) n (\alpha n_\alpha)^{1/2} A C D^{1/2} \nu^{1/2}$$

For irreversible processes, the calculated diffusion coefficient value is (15.35×10^{-5} cm²/s) for 1 wt %, (23.60×10^{-5} cm²/s) for 2 wt %, (32.74×10^{-5} cm²/s) for 3 wt %, (84.57×10^{-5} cm²/s) for 4 wt %, (7.494×10^{-5} cm²/s) for 5 wt %, and (1.643×10^{-5} cm²/s) for Ni-BTC-MOF. The maximum value of the diffusion coefficient and the R^2 value close to 1 for Ni-BTC 4 wt % rGO composite prove it to be the best material, following the controlled diffusion process with ease, as illustrated in Table 2.

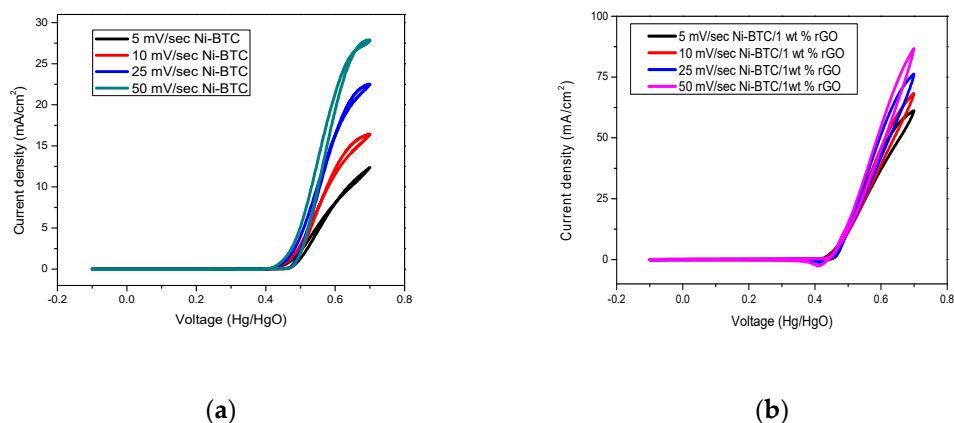


Figure 7. Cont.

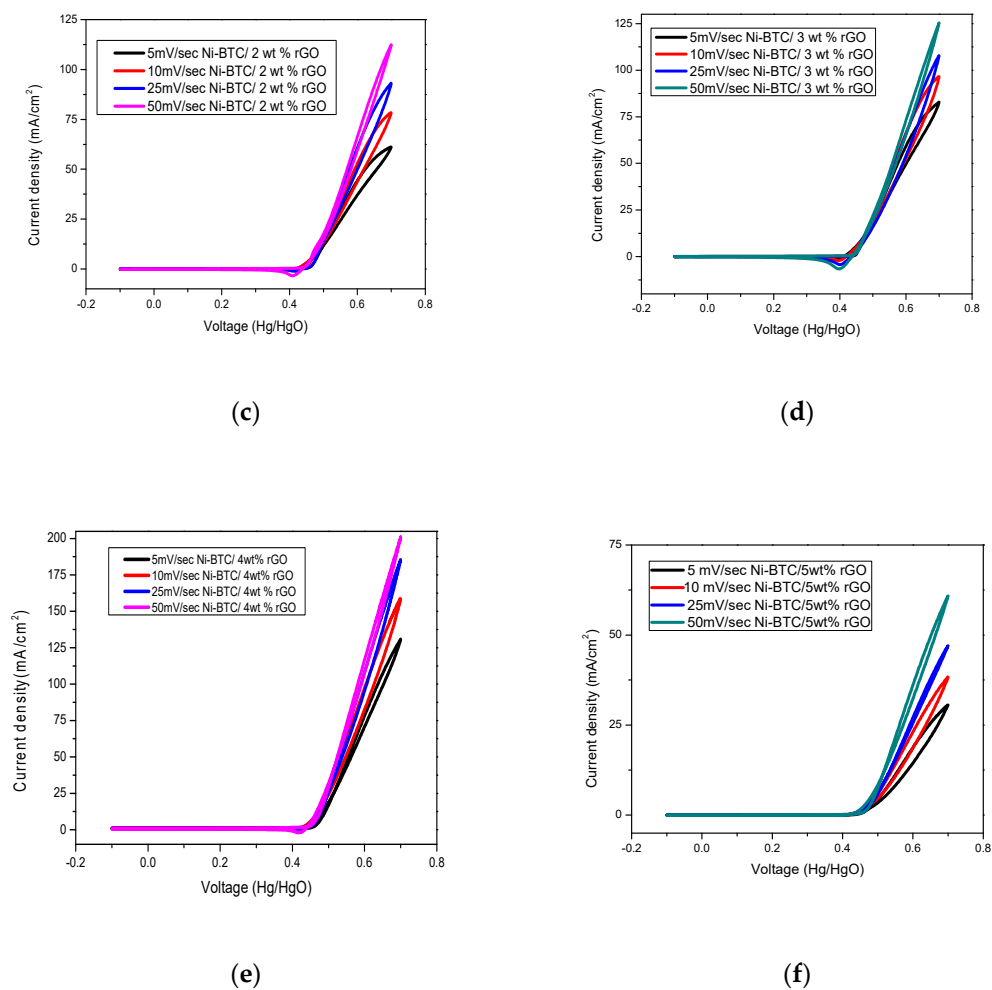


Figure 7. Comparison of effect of scan rate on current density of (a) Ni-BTC-MOF, (b) 1wt %, (c) 2 wt %, (d) 3wt %, (e) 4 wt %, and (f) 5 wt % rGO/Ni-BTC composites in 1 M NaOH and 2 M methanol solution at a scan rate of 5–50 mV/s.

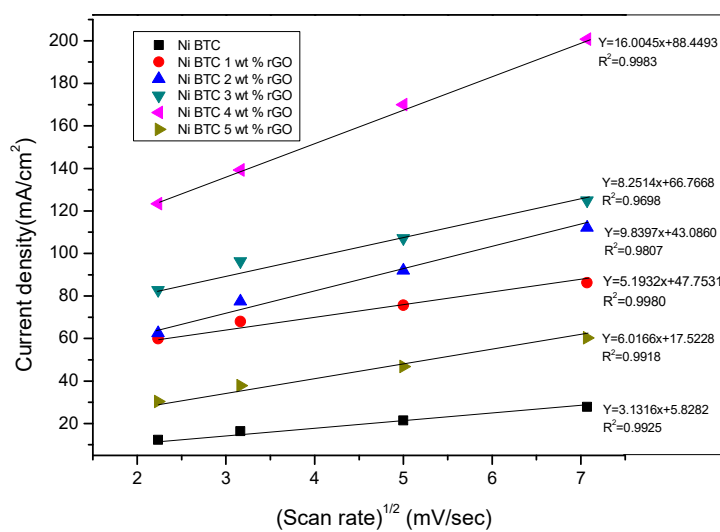


Figure 8. A plot of the linear relationship between peak current density and square root of scan rate in 1 M NaOH and 2 M methanol solution.

Table 2. Value of R^2 and diffusion coefficient of Ni-BTC-MOF and 1–5 wt % rGO composites for comparison at 50 mV/s.

Catalyst	R^2	Diffusion Co-Efficient (cm^2/s)
Ni-BTC	0.99256	1.643×10^{-5}
Ni-BTC/1 wt % rGO	0.98716	15.35×10^{-5}
Ni-BTC/2 wt % rGO	0.99269	23.60×10^{-5}
Ni-BTC/3 wt % rGO	0.98708	32.74×10^{-5}
Ni-BTC/4 wt % rGO	0.99833	84.57×10^{-5}
Ni-BTC/5 wt % rGO	0.99184	7.494×10^{-5}

The electrochemical impedance spectroscopy (EIS) is another excellent technique for investigating the catalytic activity of synthesized materials [60]. Electrochemical impedance is measured by using the potentiostatic mode in the same three-electrode system in 1 M NaOH and 2 M methanol solution with reformed GCE in the frequency range of 1– 10^5 Hz, with amplitude of 0.005 V and a peak potential of 0.69 V. In electrochemical studies, two significant factors to be considered are (a) solution resistance and (b) resistance between the reference and working electrode. Figure 9 represents the nyquist plots of all electrocatalysts, showing a distinct frequency dependent semicircle impedance curve in the high frequency region and a straight line with a slope of 45° in the low frequency region, expressing Warburg diffusion impedance. The semicircle in the high frequency region is also related to the partial oxidation of methanol to aldehyde and acid [61]. The charge transfer resistance at the electrode–electrolyte interface or the blocking properties of the rough electrode responsible for the faradic process of the ionic exchange is determined by the diameter of the semicircle. The small diameter of the semicircle indicates low charge transfer resistance (R_{ct}), and amplified reaction kinetics give an idea of the remarkable interfacial structural change, which most probably results from the high electrical conductivity of the rGO framework [62–65]. Among different rGO composites, the most efficient is Ni-BTC/4 wt % rGO composite, which has a minimum resistance toward electron and ion transfer, low activation energy, maximum approach of reactants toward active sites, and fast reaction kinetics.

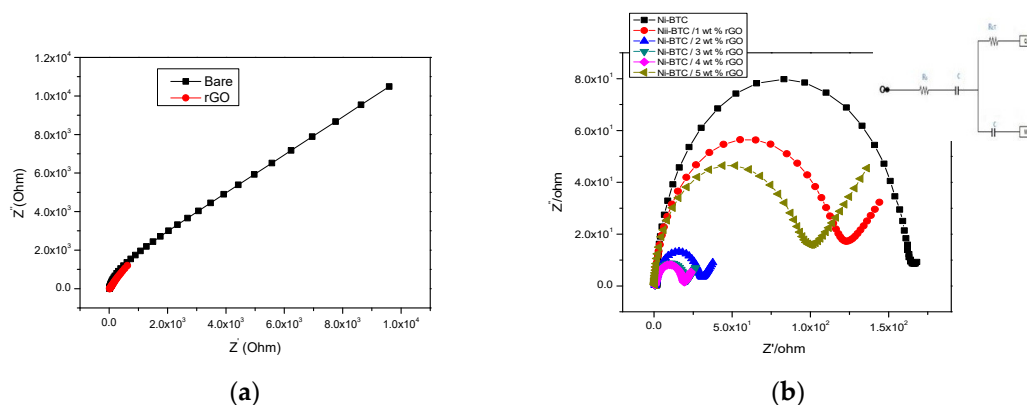
**Figure 9.** EIS comparison of (a) bare solution and rGO, and of (b) Ni-BTC-MOF and 1–5 wt % rGO composites in 1 M NaOH and 2 M methanol solution at peak potential 0.69 V.

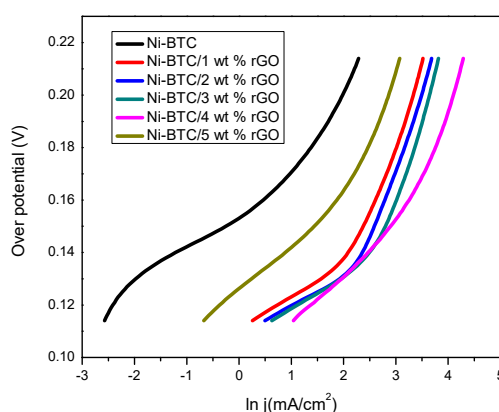
Table 3 shows a comparison of R_s and R_{ct} , and the capacitance of Ni-BTC-MOF and 1–5 wt % rGO composites.

Table 3. Electrochemical parameters from EIS data of Ni-BTC and Ni-BTC/1–5 wt % rGO composites in 1 M NaOH and 2 M methanol solution.

Sr.No	Sample	Resistance (R_s) Ohm	Resistance (R_{ct}) Ohm	Capacitance (C) Farad
1	Ni-BTC	1.340	158.00	$6.209e^{-6}$
2	Ni-BTC/1 wt % rGO	0.624	112.90	$8.316e^{-6}$
3	Ni-BTC/2 wt % rGO	0.663	28.23	$1.444e^{-5}$
4	Ni-BTC/3 wt % rGO	0.464	19.12	$1.229e^{-5}$
5	Ni-BTC/4 wt % rGO	0.328	18.12	$9.156e^{-6}$
6	Ni-BTC/5 wt % rGO	0.496	102.00	$4.728e^{-6}$

The Tafel plot helps in understanding the kinetics and reaction mechanism of the catalytic process by relating the overpotential with the natural logarithm (\ln) of current density. Overpotential is the potential exceeding the required potential for a reaction to be carried out. Among synthesized samples, the maximum current density is retained by the Ni-BTC/4 wt % rGO composite at a specific overpotential, which might be caused by the availability of reaction sites for reactants after rGO incorporation, as shown in Figure 10. The Tafel slope, representative of kinetic behavior, is calculated with the following equation [61]:

$$\eta = A + b \log i$$

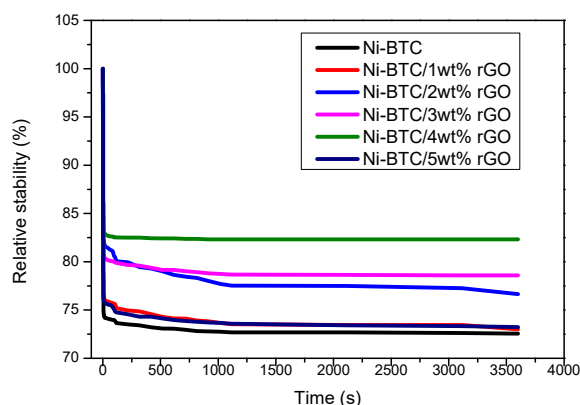
**Figure 10.** Tafel plot of Ni-BTC-MOF and 1–5 wt % rGO composites in 1 M NaOH and 2 M methanol solution at 50 mV/s.

The Tafel slope of Ni-BTC-MOF and 1–4 wt % rGO composites at low overpotential (0.14 V) is in the order of 59.75, 33.69, 29.58, 28.10, and 27.89 mV/dec, respectively. After this, the Ni-BTC-MOF/5 wt % rGO composite shows a comparatively higher Tafel slope, while at high overpotential, the Tafel slope is in the following sequence: 78.79, 36.48, 34.60, 32.57, and 29.30 mV/dec for Ni-BTC-MOF and 1–4 wt % rGO composites, respectively; followed by subsequent increase in Tafel slope for 5 wt % rGO composite to 44.41 mV/dec. Moreover, the charge transfer resistance R_{ct} is lower for 4wt% which show best activity for methanol oxidation followed by 3wt%, 2wt%, 1wt% and 5wt% rGO/Ni-BTC MOF as illustrated in Table 4. The Tafel plot is basically divided into two regions: low and high potential regions; where the reaction mechanism, or at the least rate determining step, is quite different and conveys different information. In the low potential range, methanol dehydrogenation is the main process, while oxidative removal of CO occurs in the high potential range. The low Tafel slope of Ni-BTC-MOF/4 wt % rGO composite of 27.89 mV/dec reflects faster removal of hydrogen from methanol and instant CO removal in low and high potential ranges, respectively [66–69].

Table 4. Comparison of resistance and Tafel slope of Ni-BTC and 1–5 wt % rGO composites at 50 mV/s.

Catalyst	R _{ct} (Ohm)	Tafel Slope (mV/dec)
Ni-BTC	158	59.65
Ni-BTC/1 wt % rGO	112	33.69
Ni-BTC/2 wt % rGO	28.23	29.58
Ni-BTC/3 wt % rGO	19.12	28.10
Ni-BTC/4 wt % rGO	18.12	27.89
Ni-BTC/5 wt % rGO	102	75.47

The relative stability of synthesized electrocatalytic materials was analyzed through chronoamperometric measurements by employing a three-electrode system in 1 M NaOH and 2 M methanol solution at a fixed potential of 0.69 V, as shown in Figure 11. These curve stability values do not illustrate the initial drop with 100% accuracy because of the adsorption of reaction intermediates, such as CO, COOH, and CHO, on the catalyst surface. After this, the relative stability reaches a steady state until 3600 s [70,71]. After the deployment of the set potential (i.e., 0.69 V for 3600 s), the highest stability is shown for Ni-BTC/4 wt % rGO, reaching up to 83%, which is possibly because of the 2D structure of rGO leading to high specific surface area, minimal charge transfer resistance, and tolerance to poisonous intermediates [69]. This is followed by Ni-BTC/3 wt % rGO at 80%, Ni-BTC/2 wt % rGO at 78%, Ni-BTC/1 wt % rGO at 74%, Ni-BTC/5 wt % rGO at 74.5%, and Ni-BTC at 73%. Ni-BTC-MOF shows a fast decline, in contrast to other catalysts (i.e., 1–5 wt % composites), and then shows a sluggish decline over time until reaching stability at 3600 s.

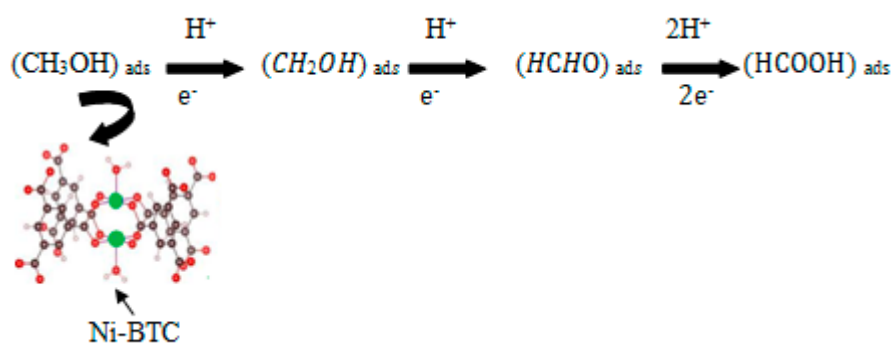
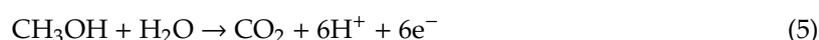
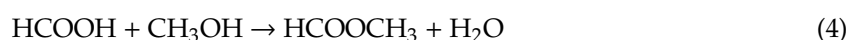
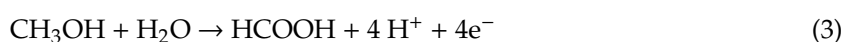
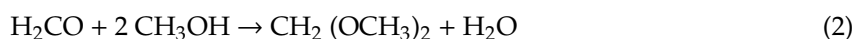
**Figure 11.** Chronoamperometry curves of Ni-BTC-MOF and 1–5 wt % rGO composites in 1 M NaOH and 2 M methanol solution at 0.69 V.

Ni-BTC-MOF/1–4 wt % rGO composites improved the electrocatalytic activity results because of the synergistic effects of rGO sheets and Ni-BTC-MOF. In the literature, subsequent elementary steps are proposed to take place during the reaction, which includes adsorption and dehydrogenation of methanol into intermediates. The overall reactions in the process are represented in Scheme 1.

Bulk Electrolysis and Product Analysis

Electrocatalytic oxidation of methanol into CO₂ can generate the maximum amount of electricity in direct methanol fuel cells, but high overpotential (0.45 V) is responsible for sluggish kinetics, even when using state-of-the-art Pt catalysts, because of poisoning of catalysts by intermediates in the oxidation process, such as CH, CH₃, and COOH [72,73]. In this work, product identification and quantification of Ni-BTC/4 wt % rGO composite's catalyzed methanol oxidation process was carried out by bulk electrolysis on a glassy carbon plate in 2 M methanol solution containing 1 M NaOH as a supporting electrolyte, as illustrated in Figure 12. At the start of the experiment, N₂ was purged for 45 min to remove oxygen, after which the potential was fixed at 0.69 V for the oxidation process.

Initially, the sharp decline in current density is because of the double layer charging process, but later on the constant current density (i.e., 199.6 mA/cm²) during bulk electrolysis for 1.5 h reflects the catalyst's stability under catalytic turnover conditions [74]. The electrolytic product was collected after a 52.7 °C charge had been passed and was further analyzed by ¹H NMR spectroscopy technique. Figure 13 symbolizes the NMR spectra of blank and Ni-BTC/4 wt % rGO composite, whereas Figure 14 represents the NMR spectra of reference electrolyte. The NMR spectra of Ni-BTC/4 wt % rGO composite after bulk electrolysis is shown in Figure 15. The possible products during bulk electrolysis are as follow:



Scheme 1. Stepwise Mechanism of methanol oxidation to formic acid.

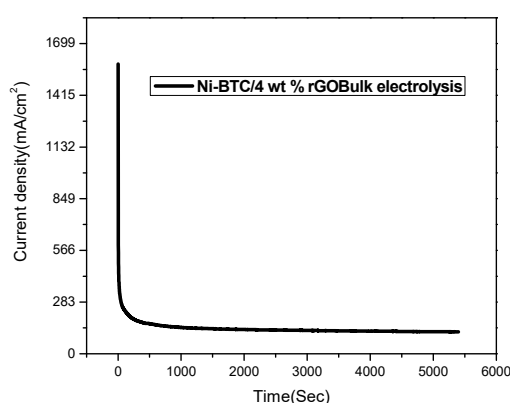


Figure 12. Bulk electrolysis of Ni-BTC/4 wt % rGO composites in 1 M NaOH and 2 M methanol solution at peak potential of 0.69 V.

According to the above equations, methanol oxidation generates formaldehyde and formic acid, which may condense with methanol to produce methyl formate and dimethoxymethane, respectively [75]. Detection of gaseous products such as CO₂ was carried out by an Agilent 7820 A gas chromatography system equipped with an Agilent HP-5 column, with dimensions of 30 m × 0.32 μm. The result was identical to CO₂ being sucked from the air and injected into the GC instrument, clarifying that CO₂ is not a final product during analysis. Qualitative analysis of liquid products such as formaldehyde and formic acid was undertaken with a Bruker DRX400 ¹H NMR spectrometer.

The final product of bulk electrolysis of catalytic material under experimental conditions was found to be formic acid, with 60.26% yield calculated through a faradic efficiency formula.

$$F.E = n \times N \times F/Q \times 100$$

where N is the number of electrons involved in the oxidation process; n is the number of moles in the product; Q is the total charge pass during bulk electrolysis; and F is Faraday's constant. The side products would be water and O₂ produced during the parallel water oxidation process.

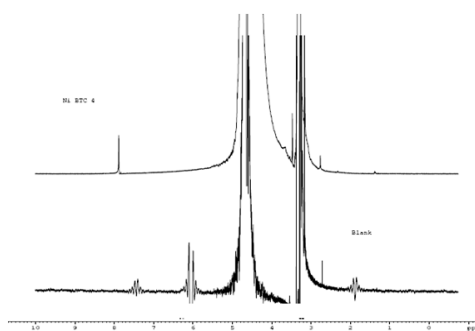


Figure 13. NMR spectra of blank and Ni-BTC/4 wt % rGO composite.

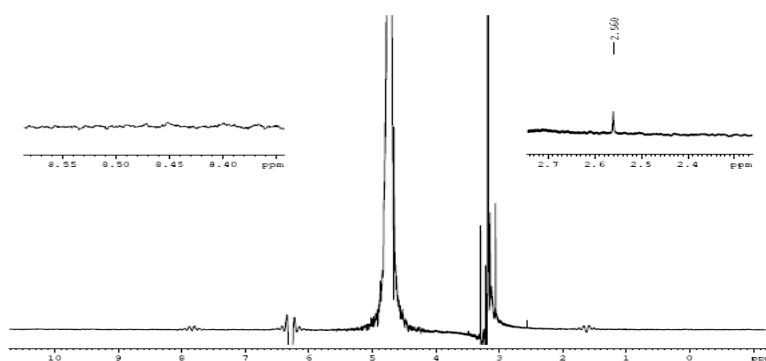


Figure 14. NMR spectra of reference electrolyte.

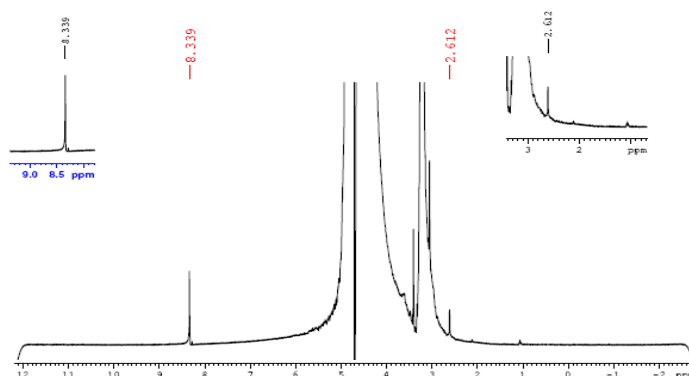


Figure 15. NMR spectra of Ni-BTC/4 wt % rGO composite after bulk electrolysis.

Table 5 below shows a comparison of synthesized MOFs and their composites with the reported materials utilized for methanol oxidation. The Ni-BTC/4 wt % rGO composite shows comparable catalytic activity to the Pt-Ni catalyst for methanol oxidation reaction (MOR) and better performance than other reported materials. This is because of the synergic effect of Ni-BTC-MOF with rGO.

Table 5. Comparison of catalytic activity of synthesized samples with reported materials.

Catalytic Materials	Methanol Concentration (M)	Catalyst Amount (mg/cm ²)	Scan Rate (mV/s)	Anodic Potential (V)	Peak Current Density (mA/cm ²)	Resistance (Ohm)	Ref.
Pt-Ni	1	20	50	1.44 vs. RHE	265.6	-	[9]
Ru@Pt/MWCNT	2	4	50	1.81 vs. RHE	182.4	606	[29]
NiCo ₂ O ₄ -rGO	0.5	-	50	1.26 vs. RHE	48.0	1000	[52]
Nanoporous Pt/Al thin films	2	-	100	0.8 vs. RHE	6.0	-	[76]
Ni-BTC	2	1.07	50	1.66 vs. RHE	27.155	158	This work
Ni-BTC/1 wt % rGO	2	1.07	50	1.66 vs. RHE	86.346	112	This work
Ni-BTC/2 wt % rGO	2	1.07	50	1.66 vs. RHE	112.04	28.23	This work
Ni-BTC/3 wt % rGO	2	1.07	50	1.66 vs. RHE	125.83	19.12	This work
Ni-BTC/4 wt % rGO	2	1.07	50	1.66 vs. RHE	200.02	18.12	This work
Ni-BTC/5 wt % rGO	2	1.07	50	1.66 vs. RHE	60.72	102	This work

3. Material and Methods

3.1. Materials

All chemicals and reagents employed for synthesis of required materials were of analytical grade and utilized without any need for further purification. Chemicals utilized for synthesis, namely Ni (NO₃)₂·6H₂O, Trimesic acid (1, 3, 5 benzene tricarboxylic acid), NaNO₃, KMnO₄, H₂O₂, and graphite powder, were purchased from Sigma Aldrich (St. Louis, MO, USA). Ethanol, DMF, H₂SO₄, hydrazine hydrate, and deionized water were bought from Merck (Kenilworth, NJ, USA).

3.2. Instrumentation

The crystal structure and phase purity of synthesized samples was confirmed using an X-ray powder diffractometer (STOE, Darmstadt, Germany) equipped with Cu K α radiation of $\lambda = 1.54060 \text{ \AA}$, within the 2θ range of 5–80°, at operational conditions of 20 kV and 5 mA, and with a step size of 4°/s. The shape and morphology was analyzed by scanning electron microscopy (VEGA3, TESCAN, Brno, Czech Republic).

The composition was confirmed via energy dispersive X-ray spectroscopy (Oxford Instruments, Abingdon, UK). Metal–ligand coordination was studied by using Spectrum 100 FTIR spectrophotometer (PerkinElmer, Waltham, MA, USA), at a wavenumber range of 500–4000 cm⁻¹.

3.3. Synthesis of Ni-BTC-MOF

Ni-BTC-MOF was synthesized through the reported solvothermal method [77]. Here, 2 g Ni (NO₃)₂·6H₂O was dissolved in 17 mL H₂O and 1 g of 1,3,5 benzene tricarboxylic acid was added to 34 mL of a mixture of C₂H₅OH and DMF solvents (1:1), followed by slow addition of the linker solution to the metal salt solution with continuous stirring for 1 h. The homogenous mixture was then transferred to a 50 mL Teflon-lined autoclave and kept in an oven at 85 °C for 24 h. After completion of the reaction, the autoclave was slowly cooled down to room temperature, the solid material was collected through filtration, followed by washing with solvents three times, and vacuum drying at 65 °C for 24 h.

3.4. Synthesis of GO and rGO

Synthesis of GO was carried out via Hummers' method [34]. Graphite powder and sodium nitrate (2:1) were first dissolved in 46 mL sulfuric acid through magnetic stirring for 1 h in an ice bath at a temperature of 5 °C. Later on, 7 g potassium permanganate (KMnO₄) was gradually added at the same condition, followed by 6 h continuous stirring at 35 °C. Then, 80 mL deionized (DI) water was slowly added to the brown paste in such a way that the temperature was not allowed to rise above 60 °C. Moreover, dilution was achieved through addition of 200 mL DI water, and finally the reaction was stopped after addition of 10 mL 30% H₂O₂. The reaction mixture was repeatedly washed with

diluted HCl and DI water through centrifugation to ensure a pH of 6–7. Sonication was done to obtain exfoliated GO, and the product was then vacuum dried at 45 °C for 24 h.

In order to prepare rGO, 100 mg GO was dissolved in 100 mL DI water and sonicated for 2 h to obtain a homogenous mixture. Hydrazine hydrate (1 mL) was then added to the reaction mixture and refluxed for 24 h at 100 °C. Hydrophobic rGO appeared on the surface after completion of the reaction. The porous, blackish product was filtered and washed with DI water and ethanol, followed by vacuum drying at 45 °C [33].

3.5. Synthesis of Ni-BTC-MOF/rGO Composites

A series of rGO composites of Ni-BTC-MOF were synthesized using the abovementioned procedure. A linker solution prepared in DMF and ethanol was slowly added to the metal salt aqueous solution and stirred for 1 h. Subsequently, an appropriate amount of rGO was added to the MOF solution, followed by 2 h sonication to acquire a homogenous mixture. After this, the reaction mixture was poured into a Teflon-lined autoclave and kept in an oven for 24 h at 85 °C. The obtained solid product was then repeatedly washed with a mixture of solvents and dried in a vacuum at 65 °C for 24 h. The layout of synthesis scheme is given in Figure 16.

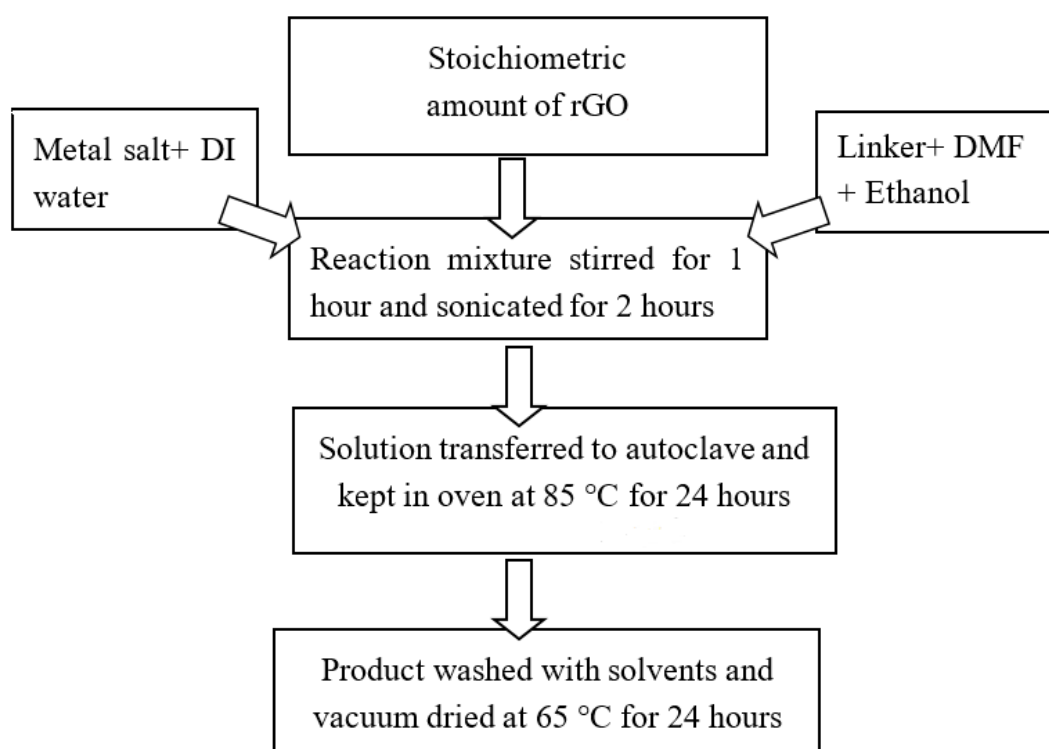


Figure 16. Synthetic procedure of Ni-BTC-MOF and 1–5 wt % rGO composites.

4. Conclusions

Ni-BTC-MOF and its 1–5 wt % rGO composites synthesized by the solvothermal method were analyzed for methanol oxidation in alkaline media. The as-prepared samples exhibited remarkable potential for formic acid production during this oxidation process, particularly the Ni-BTC/4 wt % rGO composite shows highest activity. The loading amount of the highly efficient Ni-BTC/4 wt % rGO composite was four times less than the state-of-the-art Pt metal, with a current density of 200.22 mA/cm² at a peak potential of 0.69 V versus Hg/HgO. It also possessed a low Tafel slope (27.89 mV/dec) and minimal resistance (18.12 Ohm), making it an efficient alternate to expensive materials that are utilized for selective oxidation of methanol to formic acid in direct methanol fuel cells.

Author Contributions: Conceptualization, L.Y. and T.N.; data curation, methodology, and investigation, L.Y. and N.Z.; supervision T.N., H.N., and N.I.; original draft preparation, L.Y.; writing—reviews and editing, all authors.

Funding: Financial support received from Higher Education Commission (HEC) Pakistan under its National Research Program for Universities (NRPU), project no. 6013, is greatly acknowledged.

Acknowledgments: The author would like to acknowledge the School of Chemical and Material Engineering (SCME), School of Natural Sciences (SNS), and U.S.–Pakistan School for Advance Studies in Energy (USPCAS-E) at NUST for providing the lab facilities.

Conflicts of Interest: The authors declare no conflict of interest.

References

1. Dincer, I. Renewable energy and sustainable development: A crucial review. *Renew. Sustain. Energy Rev.* **2000**, *4*, 157–175. [\[CrossRef\]](#)
2. Mintsouli, I.; Georgieva, J.; Armanyanov, S.; Valova, E.; Avdeev, G.; Hubin, A.; Steenhaut, O.; Dille, J.; Tsiplakides, D.; Balomenou, S. Pt-Cu electrocatalysts for methanol oxidation prepared by partial galvanic replacement of Cu/carbon powder precursors. *Appl. Catal. B Environ.* **2013**, *136*, 160–167. [\[CrossRef\]](#)
3. Appleby, A.J. *Fuel Cell Handbook*; Krieger Pub Co.: Malabar, FL, USA, 1989.
4. Steele, B.; Heinzl, A. Materials for fuel-cell technologies. *Nature* **2001**, *414*, 345–352. [\[CrossRef\]](#)
5. Franceschini, E.A.; Bruno, M.M.; Williams, F.J.; Viva, F.A.; Corti, H.R. High-activity mesoporous Pt/Ru catalysts for methanol oxidation. *ACS Appl. Mater. Interfaces* **2013**, *5*, 10437–10444. [\[CrossRef\]](#)
6. Tian, G.L.; Zhang, Q.; Zhang, B.; Jin, Y.G.; Huang, J.Q.; Su, D.S.; Wei, F. Toward full exposure of “active sites”: Nanocarbon electrocatalyst with surface enriched nitrogen for superior oxygen reduction and evolution reactivity. *Adv. Funct. Mater.* **2014**, *24*, 5956–5961. [\[CrossRef\]](#)
7. Kaichev, V.V.; Popova, G.Y.; Chesalov, Y.A.; Saraev, A.; Zemlyanov, D.; Beloshapkin, S.; Knop-Gericke, A.; Schlögl, R.; Andrushkevich, T.; Bukhtiyarov, V. Selective oxidation of methanol to form dimethoxymethane and methyl formate over a monolayer V₂O₅/TiO₂ catalyst. *J. Catal.* **2014**, *311*, 59–70. [\[CrossRef\]](#)
8. Kakati, N.; Maiti, J.; Lee, S.H.; Jee, S.H.; Viswanathan, B.; Yoon, Y.S. Anode catalysts for direct methanol fuel cells in acidic media: Do we have any alternative for Pt or Pt–Ru? *Chem. Rev.* **2014**, *114*, 12397–12429. [\[CrossRef\]](#)
9. Mathe, N.R.; Scriba, M.R.; Rikhotso, R.S.; Coville, N.J. Microwave-irradiation polyol synthesis of PVP-protected Pt–Ni electrocatalysts for methanol oxidation reaction. *Electrocatalysis* **2018**, *9*, 388–399. [\[CrossRef\]](#)
10. Li, W.; Liang, C.; Qiu, J.; Zhou, W.; Han, H.; Wei, Z.; Sun, G.; Xin, Q. Carbon nanotubes as support for cathode catalyst of a direct methanol fuel cell. *Carbon* **2002**, *40*, 787–790. [\[CrossRef\]](#)
11. Mehek, R.; Iqbal, N.; Noor, T.; Nasir, H.; Mehmood, Y.; Ahmed, S. Novel Co-MOF/graphene oxide electrocatalyst for methanol oxidation. *Electrochim. Acta* **2017**, *255*, 195–204. [\[CrossRef\]](#)
12. Heli, H.; Jafarian, M.; Mahjani, M.; Gobal, F. Electro-oxidation of methanol on copper in alkaline solution. *Electrochim. Acta* **2004**, *49*, 4999–5006. [\[CrossRef\]](#)
13. Liu, F.; Lee, J.Y.; Zhou, W. Multi-Segment Pt–RuNi Nanorods for Methanol Electro-Oxidation at Room Temperature. *J. Electrochem. Soc.* **2006**, *153*, A2133–A2138. [\[CrossRef\]](#)
14. He, Y.-B.; Li, G.-R.; Wang, Z.-L.; Ou, Y.-N.; Tong, Y.-X. Pt nanorods aggregates with enhanced electrocatalytic activity toward methanol oxidation. *J. Phys. Chem. C* **2010**, *114*, 19175–19181. [\[CrossRef\]](#)
15. Alia, S.M.; Zhang, G.; Kisailus, D.; Li, D.; Gu, S.; Jensen, K.; Yan, Y. Porous platinum nanotubes for oxygen reduction and methanol oxidation reactions. *Adv. Funct. Mater.* **2010**, *20*, 3742–3746. [\[CrossRef\]](#)
16. Varela, F.R.; Savadogo, O. The effect of anode catalysts on the behavior of low temperature direct propane polymer electrolyte fuel cells (DPFC). *J. New Mater. Electrochem. Syst.* **2006**, *9*, 127.
17. Cai, Z.; Martin, C.R. Electronically conductive polymer fibers with mesoscopic diameters show enhanced electronic conductivities. *J. Am. Chem. Soc.* **1989**, *111*, 4138–4139. [\[CrossRef\]](#)
18. Hsin, Y.L.; Hwang, K.C.; Yeh, C.-T. Poly (vinylpyrrolidone)-modified graphite carbon nanofibers as promising supports for PtRu catalysts in direct methanol fuel cells. *J. Am. Chem. Soc.* **2007**, *129*, 9999–10010. [\[CrossRef\]](#)
19. Li, Y.; Gao, W.; Ci, L.; Wang, C.; Ajayan, P.M. Catalytic performance of Pt nanoparticles on reduced graphene oxide for methanol electro-oxidation. *Carbon* **2010**, *48*, 1124–1130. [\[CrossRef\]](#)
20. Zhu, Q.-L.; Xu, Q. Metal–organic framework composites. *Chem. Soc. Rev.* **2014**, *43*, 5468–5512. [\[CrossRef\]](#)
21. Huang, X.; Qi, X.; Boey, F.; Zhang, H. Graphene-based composites. *Chem. Soc. Rev.* **2012**, *41*, 666–686. [\[CrossRef\]](#)

22. Stock, N.; Biswas, S. Synthesis of metal-organic frameworks (MOFs): Routes to various MOF topologies, morphologies, and composites. *Chem. Rev.* **2011**, *112*, 933–969. [[CrossRef](#)] [[PubMed](#)]
23. Kim, J.; Yeo, S.; Jeon, J.-D.; Kwak, S.-Y. Enhancement of hydrogen storage capacity and hydrostability of metal-organic frameworks (MOFs) with surface-loaded platinum nanoparticles and carbon black. *Microporous Mesoporous Mater.* **2015**, *202*, 8–15. [[CrossRef](#)]
24. Khan, I.A.; Badshah, A.; Nadeem, M.A.; Haider, N.; Nadeem, M.A. A copper based metal-organic framework as single source for the synthesis of electrode materials for high-performance supercapacitors and glucose sensing applications. *Int. J. Hydrogen Energy* **2014**, *39*, 19609–19620. [[CrossRef](#)]
25. Jahan, M.; Liu, Z.; Loh, K.P. A Graphene oxide and copper-centered metal organic framework composite as a tri-functional catalyst for HER, OER, and ORR. *Adv. Funct. Mater.* **2013**, *23*, 5363–5372. [[CrossRef](#)]
26. Tang, H.; Cai, S.; Xie, S.; Wang, Z.; Tong, Y.; Pan, M.; Lu, X. Metal-organic-framework-derived dual metal- and nitrogen-doped carbon as efficient and robust oxygen reduction reaction catalysts for microbial fuel cells. *Adv. Sci.* **2016**, *3*, 1500265. [[CrossRef](#)]
27. Ma, T.Y.; Dai, S.; Jaroniec, M.; Qiao, S.Z. Metal-organic framework derived hybrid Co₃O₄-carbon porous nanowire arrays as reversible oxygen evolution electrodes. *J. Am. Chem. Soc.* **2014**, *136*, 13925–13931. [[CrossRef](#)]
28. Fu, Y.; Sun, D.; Chen, Y.; Huang, R.; Ding, Z.; Fu, X.; Li, Z. An amine-functionalized titanium metal-organic framework photocatalyst with visible-light-induced activity for CO₂ reduction. *Angew. Chem. Int. Ed.* **2012**, *51*, 3364–3367. [[CrossRef](#)]
29. Dang, L.Q.; Nguyen, M.T.; Van Truong, N.; Le, P.H.; Long, N. Investigation of Carbon Supported Ru-Pt Nanoparticles for High-Performance Electrocatalytic Oxidation of Methanol. *Int. J. Electrochem. Sci.* **2017**, *12*, 10187–10198. [[CrossRef](#)]
30. Behmenyar, G.; Akin, A.N. Investigation of carbon supported Pd-Cu nanoparticles as anode catalysts for direct borohydride fuel cell. *J. Power Sources* **2014**, *249*, 239–246. [[CrossRef](#)]
31. Song, G.; Wang, Z.; Wang, L.; Li, G.; Huang, M.; Yin, F. Preparation of MOF (Fe) and its catalytic activity for oxygen reduction reaction in an alkaline electrolyte. *Chin. J. Catal.* **2014**, *35*, 185–195. [[CrossRef](#)]
32. Hanif, S.; Shi, X.; Iqbal, N.; Noor, T.; Anwar, R.; Kannan, A. ZIF derived PtNiCo/NC cathode catalyst for proton exchange membrane fuel cell. *Appl. Catal. B Environ.* **2019**, *258*, 117947. [[CrossRef](#)]
33. Noor, T.; Zaman, N.; Nasir, H.; Iqbal, N.; Hussain, Z. Electro catalytic study of NiO-MOF/rGO composites for methanol oxidation reaction. *Electrochim. Acta* **2019**, *307*, 1–12. [[CrossRef](#)]
34. Noor, T.; Ammad, M.; Zaman, N.; Iqbal, N.; Yaqoob, L.; Nasir, H. A Highly Efficient and Stable Copper BTC Metal Organic Framework Derived Electrocatalyst for Oxidation of Methanol in DMFC Application. *Catal. Lett.* **2019**, 1–16. [[CrossRef](#)]
35. Sarwar, E.; Noor, T.; Iqbal, N.; Mehmood, Y.; Ahmed, S.; Mehek, R. Effect of Co-Ni Ratio in Graphene Based Bimetallic Electro-catalyst for Methanol Oxidation. *Fuel Cells* **2018**, *18*, 189–194. [[CrossRef](#)]
36. Rahim, M.A.; Hameed, R.A.; Khalil, M. Nickel as a catalyst for the electro-oxidation of methanol in alkaline medium. *J. Power Sources* **2004**, *134*, 160–169. [[CrossRef](#)]
37. Sreepasad, T.; Maliyekkal, S.M.; Lisha, K.; Pradeep, T. Reduced graphene oxide-metal/metal oxide composites: Facile synthesis and application in water purification. *J. Hazard. Mater.* **2011**, *186*, 921–931. [[CrossRef](#)]
38. Krishnamoorthy, K.; Jeyasubramanian, K.; Premanathan, M.; Subbiah, G.; Shin, H.S.; Kim, S.J. Graphene oxide nanopaint. *Carbon* **2014**, *72*, 328–337. [[CrossRef](#)]
39. Zhou, L.; Kong, X.; Gao, M.; Lian, F.; Li, B.; Zhou, Z.; Cao, H. Hydrothermal fabrication of MnCO₃@ rGO composite as an anode material for high-performance lithium ion batteries. *Inorg. Chem.* **2014**, *53*, 9228–9234. [[CrossRef](#)]
40. Petit, C.; Bandoz, T.J. MOF-graphite oxide composites: Combining the uniqueness of graphene layers and metal-organic frameworks. *Adv. Mater.* **2009**, *21*, 4753–4757. [[CrossRef](#)]
41. Israr, F.; Kim, D.K.; Kim, Y.; Oh, S.J.; Ng, K.C.; Chun, W. Cost effective and low energy consuming hydrothermal synthesis of Ni based MOF. *J. Energ. Eng.* **2015**, *24*, 51–54. [[CrossRef](#)]
42. Israr, F.; Chun, D.; Kim, Y.; Kim, D.K. High yield synthesis of Ni-BTC metal-organic framework with ultrasonic irradiation: Role of polar aprotic DMF solvent. *Ultrason. Sonochem.* **2016**, *31*, 93–101. [[CrossRef](#)] [[PubMed](#)]

43. Yaghi, O.; Li, H.; Groy, T. Construction of porous solids from hydrogen-bonded metal complexes of 1, 3, 5-benzenetricarboxylic acid. *J. Am. Chem. Soc.* **1996**, *118*, 9096–9101. [[CrossRef](#)]
44. Jabbarian, S.; Ghaffarinejad, A. Electrochemical Synthesis of NiBTC Metal Organic Framework Thin Layer on Nickel Foam: An Efficient Electrocatalyst for the Hydrogen Evolution Reaction. *J. Inorg. Organomet. Polym. Mater.* **2019**, *29*, 1565–1574. [[CrossRef](#)]
45. Jabbar, A.; Yasin, G.; Khan, W.Q.; Anwar, M.Y.; Korai, R.M.; Nizam, M.N.; Muhyodin, G. Electrochemical deposition of nickel graphene composite coatings: Effect of deposition temperature on its surface morphology and corrosion resistance. *RSC Adv.* **2017**, *7*, 31100–31109. [[CrossRef](#)]
46. Andrijanto, E.; Shoelarta, S.; Subiyanto, G.; Rifki, S. Facile synthesis of graphene from graphite using ascorbic acid as reducing agent. In Proceedings of the AIP ICAMST 2015 Conference, Semarang, Indonesia, 6–7 October 2015.
47. Zhang, Y.; Liu, H.; Zhu, Z.; Wong, K.-W.; Mi, R.; Mei, J.; Lau, W.-M. A green hydrothermal approach for the preparation of graphene/ α -MnO₂ 3D network as anode for lithium ion battery. *Electrochim. Acta* **2013**, *108*, 465–471. [[CrossRef](#)]
48. Zeng, G.; Chen, Y.; Chen, L.; Xiong, P.; Wei, M. Hierarchical cerium oxide derived from metal-organic frameworks for high performance supercapacitor electrodes. *Electrochim. Acta* **2016**, *222*, 773–780. [[CrossRef](#)]
49. Sun, K.; Li, L.; Yu, X.; Liu, L.; Meng, Q.; Wang, F.; Zhang, R. Functionalization of mixed ligand metal-organic frameworks as the transport vehicles for drugs. *J. Colloid Interface Sci.* **2017**, *486*, 128–135. [[CrossRef](#)]
50. Wu, Y.; Song, X.; Li, S.; Zhang, J.; Yang, X.; Shen, P.; Gao, L.; Wei, R.; Zhang, J.; Xiao, G. 3D-monoclinic M–BTC MOF (M= Mn, Co, Ni) as highly efficient catalysts for chemical fixation of CO₂ into cyclic carbonates. *J. Ind. Eng. Chem.* **2018**, *58*, 296–303. [[CrossRef](#)]
51. Hamidipour, L.; Farzaneh, F. Cobalt metal organic framework as an efficient heterogeneous catalyst for the oxidation of alkanes and alkenes. *React. Kinet. Mech. Catal.* **2013**, *109*, 67–75. [[CrossRef](#)]
52. Machado, B.F.; Serp, P. Graphene-based materials for catalysis. *Catal. Sci. Technol.* **2012**, *2*, 54–75. [[CrossRef](#)]
53. Hidayah, N.; Liu, W.-W.; Lai, C.-W.; Noriman, N.; Khe, C.-S.; Hashim, U.; Lee, H.C. Comparison on graphite, graphene oxide and reduced graphene oxide: Synthesis and characterization. *AIP Conf. Proc.* **2017**, *1892*, 150002.
54. Feng, H.; Cheng, R.; Zhao, X.; Duan, X.; Li, J. A low-temperature method to produce highly reduced graphene oxide. *Nat. Commun.* **2013**, *4*, 1539. [[CrossRef](#)] [[PubMed](#)]
55. Antolini, E.; Salgado, J.R.; Gonzalez, E.R. The methanol oxidation reaction on platinum alloys with the first row transition metals: The case of Pt–Co and–Ni alloy electrocatalysts for DMFCs: A short review. *Appl. Catal. B Environ.* **2006**, *149*, 137–149. [[CrossRef](#)]
56. Cordeiro, C.; De Vries, M.; Cremers, T.; Westerink, B. The role of surface availability in membrane-induced selectivity for amperometric enzyme-based biosensors. *Sens. Actuators B Chem.* **2016**, *223*, 679–688. [[CrossRef](#)]
57. Das, A.K.; Layek, R.K.; Kim, N.H.; Jung, D.; Lee, J.H. Reduced graphene oxide (RGO)-supported NiCo₂O₄ nanoparticles: An electrocatalyst for methanol oxidation. *Nanoscale* **2014**, *6*, 10657–10665. [[CrossRef](#)]
58. Zhu, D.; Guo, C.; Liu, J.; Wang, L.; Du, Y.; Qiao, S.-Z. Two-dimensional metal–organic frameworks with high oxidation states for efficient electrocatalytic urea oxidation. *Chem. Commun.* **2017**, *53*, 10906–10909. [[CrossRef](#)]
59. Zhang, X.; Jiang, Z.H.; Yao, Z.P.; Song, Y.; Wu, Z.D. Effects of scan rate on the potentiodynamic polarization curve obtained to determine the Tafel slopes and corrosion current density. *Corros. Sci.* **2009**, *51*, 581–587. [[CrossRef](#)]
60. Parwaiz, S.; Bhunia, K.; Das, A.K.; Khan, M.M.; Pradhan, D. Cobalt-doped ceria/reduced graphene oxide nanocomposite as an efficient oxygen reduction reaction catalyst and supercapacitor material. *J. Phys. Chem. C* **2017**, *121*, 20165–20176. [[CrossRef](#)]
61. Huang, T.; Mao, S.; Zhou, G.; Zhang, Z.; Wen, Z.; Huang, X.; Ci, S.; Chen, J. A high-performance catalyst support for methanol oxidation with graphene and vanadium carbonitride. *Nanoscale* **2015**, *7*, 1301–1307. [[CrossRef](#)]
62. Yu, E.H.; Scott, K.; Reeve, R.W. A study of the anodic oxidation of methanol on Pt in alkaline solutions. *J. Electroanal. Chem.* **2003**, *547*, 17–24. [[CrossRef](#)]
63. Niu, L.; Li, Q.; Wei, F.; Chen, X.; Wang, H. Electrochemical impedance and morphological characterization of platinum-modified polyaniline film electrodes and their electrocatalytic activity for methanol oxidation. *J. Electroanal. Chem.* **2003**, *544*, 121–128. [[CrossRef](#)]

64. Zhu, X.; Zhang, P.; Xu, S.; Yan, X.; Xue, Q. Free-standing three-dimensional graphene/manganese oxide hybrids as binder-free electrode materials for energy storage applications. *ACS Appl. Mater. Interfaces* **2014**, *6*, 11665–11674. [[CrossRef](#)] [[PubMed](#)]
65. Wu, Q.; Jiang, M.; Zhang, X.; Cai, J.; Lin, S. A novel octahedral MnO/RGO composite prepared by thermal decomposition as a noble-metal free electrocatalyst for ORR. *J. Mater. Sci.* **2017**, *52*, 6656–6669. [[CrossRef](#)]
66. Wang, W.; Li, Y.; Wang, H. Tin oxide nanoparticle-modified commercial PtRu catalyst for methanol oxidation. *Micro Nano Lett.* **2013**, *8*, 23–26. [[CrossRef](#)]
67. Huang, Y.; Cai, J.; Liu, M.; Guo, Y. Fabrication of a novel PtPbBi/C catalyst for ethanol electro-oxidation in alkaline medium. *Electrochim. Acta* **2012**, *83*, 1–6. [[CrossRef](#)]
68. Wang, H.; Da, H.; Wang, R.; Ji, S. Beef-derived mesoporous carbon as highly efficient support for PtRuIr electrocatalysts and their high activity for CO and methanol oxidation. *S. Afr. J. Chem.* **2014**, *67*, 33–39.
69. Ye, W.; Zhang, X.; Chen, Y.; Du, Y.; Zhou, F.; Wang, C. Pulsed electrodeposition of reduced graphene oxide on glass carbon electrode as an effective support of electrodeposited Pt microspherical particles: Nucleation studies and the application for methanol electro-oxidation. *Int. J. Electrochem. Sci.* **2013**, *8*, e2139.
70. Huang, W.; Wang, H.; Zhou, J.; Wang, J.; Duchesne, P.N.; Muir, D.; Zhang, P.; Han, N.; Zhao, F.; Zeng, M. Highly active and durable methanol oxidation electrocatalyst based on the synergy of platinum–nickel hydroxide–graphene. *Nat. Commun.* **2015**, *6*, 10035. [[CrossRef](#)]
71. Zheng, Y.; Chen, H.; Dai, Y.; Zhang, N.; Zhao, W.; Wang, S.; Lou, Y.; Li, Y.; Sun, Y. Preparation and characterization of Pt/TiO₂ nanofibers catalysts for methanol electro-oxidation. *Electrochim. Acta* **2015**, *178*, 74–79. [[CrossRef](#)]
72. Vigier, F.; Rousseau, S.; Coutanceau, C.; Leger, J.-M.; Lamy, C. Electrocatalysis for the direct alcohol fuel cell. *Top. Catal.* **2006**, *40*, 111–121. [[CrossRef](#)]
73. Asiri, H.A.; Anderson, A.B. Mechanisms for ethanol electrooxidation on Pt (111) and adsorption bond strengths defining an ideal catalyst. *J. Electrochem. Soc.* **2015**, *162*, F115–F122. [[CrossRef](#)]
74. Yang, Y.; McElwee-White, L. Electrochemical oxidation of methanol using dppm-bridged Ru/Pd, Ru/Pt and Ru/Au catalysts. *Dalton Trans.* **2004**, *15*, 2352–2356. [[CrossRef](#)]
75. Liu, Y.; Zhao, S.-F.; Guo, S.-X.; Bond, A.M.; Zhang, J.; Zhu, G.; Hill, C.L.; Geletii, Y.V. Electrooxidation of Ethanol and Methanol Using the Molecular Catalyst $[\{\text{Ru}_4\text{O}_4(\text{OH})_2(\text{H}_2\text{O})_4\}(\gamma\text{-SiW}_{10}\text{O}_{36})_2]^{10-}$. *J. Am. Chem. Soc.* **2016**, *138*, 2617–2628. [[CrossRef](#)] [[PubMed](#)]
76. Nahm, C.; Kim, C.; Park, Y.; Park, B. Nanoporous Pt thin films with superior catalytic activities by the electrochemical dissolution of Al. *Met. Mater. Int.* **2009**, *15*, 989–992. [[CrossRef](#)]
77. Nguyen, T.; Thuy, V.; Luu, C.L.; Hoang, T.C.; Nguyen, T.; Bui, T.H.; Duy, N.; Phuc, H.; Pham, T.; Thuy, P. Synthesis of MOF-199 and application to CO₂ adsorption. *Adv. Nat. Sci. Nanosci. Nanotechnol. (Online)* **2013**, *4*. [[CrossRef](#)]

